Article:
Suhr, B. orcid.org/0000-0002-0259-4418, Skipper, W.A. orcid.org/0000-0001-8315-2656, Lewis, R. orcid.org/0000-0002-4300-0540 et al. (1 more author) (2024) DEM simulation of single sand grain crushing in sanded wheel–rail contacts. Powder Technology, 432. 119150. ISSN: 0032-5910

https://doi.org/10.1016/j.powtec.2023.119150

Powder Technology 432 (2024) 119150

Contents lists available at ScienceDirect

Powder Technology

journal homepage: www.journals.elsevier.com/powder-technology

DEM simulation of single sand grain crushing in sanded wheel–rail contacts

Bettina Suhr [a], William A. Skipper [b,*], Roger Lewis [b], Klaus Six [a]

[a] Virtual Vehicle Research GmbH, Inffeldgasse 21/A, Graz, 8010, Austria
[b] The University of Sheffield, Department of Mechanical Engineering, Mappin Street, Sheffield, S1 3JD, UK

HIGHLIGHTS

- Sanding process: sands grains fracture when entering the wheel–rail contact.
- Single grain crushing tests: two sands, dry/wet contact, 900 MPa contact pressure.
- Different spread of fragments and formation of solidified clusters at high load.
- DEM model development: particle breakage and material behaviour at high load.
- Successful calibration of DEM model for both sand types and contact conditions.

GRAPHICAL ABSTRACT

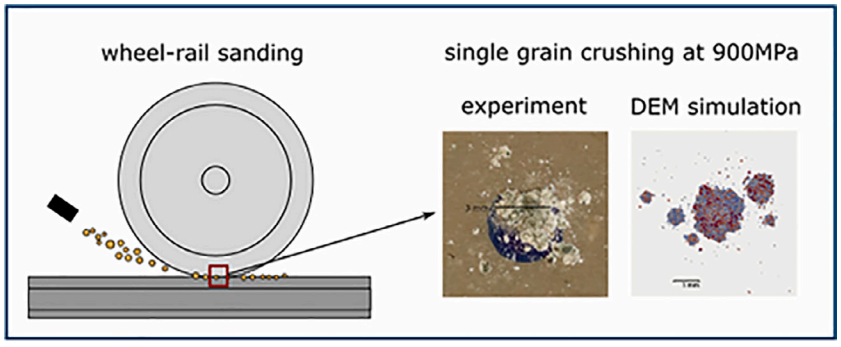

ARTICLE INFO

Dataset link: zenodo.org

Keywords:
Single grain crushing
DEM modelling
High loads
Sanded wheel–rail contact

ABSTRACT

In railways, low adhesion conditions lead to problems in braking and traction. Sanding increases adhesion by blasting sand grains towards the wheel–rail contact. Which physical mechanisms increase adhesion during sanding is poorly understood, as research in this field has been almost exclusively experimental. This work is the first step in developing a DEM model describing the sanding process. Previous experimental studies involve single grain crushing tests focusing on initial breakage and repeated breakage under realistic wheel–rail contact pressures of 900 MPa. Tests on two types of rail sand under dry and wet contact conditions, showed different spread of fragments as well as the formation of clusters of solidified fragments at high stresses. The developed DEM model captures the observed behaviour for both types of sand, and both contact conditions. Combining experimental research and DEM modelling aims to improve the understanding of adhesion increasing mechanisms in sanded wheel–rail contacts.

1. Introduction

For many years, sanding of wheel–rail contacts has been used to overcome low adhesion conditions. The maximal adhesion coefficient (AC) limits the transferable tangential force in the contact. In general, the wheel–rail contact is characterised by an extremely high normal stress, up to 900 MPa, accompanied by extremely high tangential stresses, which are caused e.g. by traction or braking. This results in severe plastic deformation of the near-surface layers [1], damage, wear and a roughness change of both wheel and rail, which affects the AC. The contact condition has a large influence on the AC. Under dry conditions, the AC is around 0.35 or higher [2,3]. So-called third body layers (3BLs) can be embedded between wheel and rail: liquids (e.g. water, oil), solids (e.g. leaves, wear particles, iron oxides or even sand fragments) or combinations thereof. Under some contact conditions low adhesion occurs, e.g. damp (wet) contact conditions [4] ('wet rail' phenomenon) or when the rail surface is contaminated with

* Corresponding author.
E-mail addresses: bettina.suhr@v2c2.at (B. Suhr), w.skipper@sheffield.ac.uk (W.A. Skipper), roger.lewis@sheffield.ac.uk (R. Lewis), klaus.six@v2c2.at (K. Six).

https://doi.org/10.1016/j.powtec.2023.119150
Received 21 August 2023; Received in revised form 24 October 2023; Accepted 12 November 2023
Available online 17 November 2023

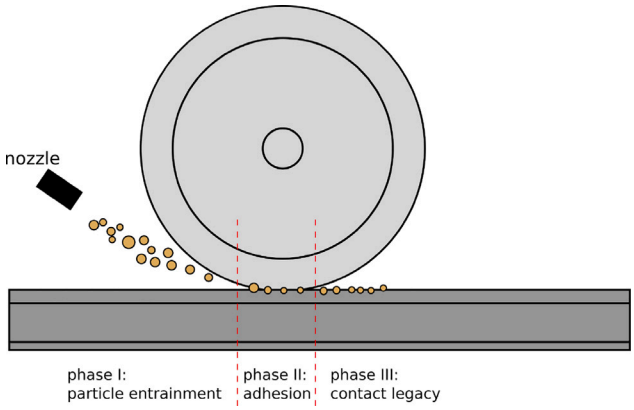

Fig. 1. Phases during wheel–rail contact sanding.

leaves [5,6]. In such cases, the AC is below 0.1 [7,8] and this directly influences the traction and braking behaviour of railway vehicles in service. Therefore, low adhesion can cause safety issues in the worst case [6,9].

Under low adhesion conditions, the AC can be increased by spraying sand from a nozzle towards the wheel–rail contact. The process can be divided into three phases, see Fig. 1. In phase I, the particles are applied: some are expelled and some are entrained into the contact. In phase II, particles fracture repeatedly in the wheel–rail contact and influence the adhesion. Finally, in phase III particles leave the contact and some of them remain on wheel and rail. While sanding does increase the AC under low adhesion conditions, it can also lead to increased damage on both wheel and rail [10,11].

Wheel–rail sanding is a field of active research, where the adhesion increasing aspect is more extensively investigated [12] than the damage or isolation aspect [13]. This research has been almost purely experimental, e.g. measuring adhesion coefficients (ACs) under different contact conditions (dry, wet, ...) applying different sands or other particles.

Despite the active research in this field, the physical mechanisms causing the change in ACs under sanded conditions are still poorly understood. When entering the contact, sand grains will fracture repeatedly and some of their fragments will be expelled. The amount of sand in the contact determines whether the metal surfaces are (partially) separated or not, allowing for different mechanisms of load transfer, see Fig. 2. Under high loads sand fragments solidify and form clusters, which indent into wheel and rail surfaces (affecting roughness) [14]. Adhesion could also be increased via form closure effects, or the sand powder solidifies and partially covers the rough wheel–rail surfaces, increasing the effective contact area between sand and steel and thereby the AC. The role of water in wet contacts is also unclear. This mentioned lack of understanding is caused by the fact that current experimental abilities do not allow for any monitoring of the aforementioned mechanisms in the contact zone during roll-over.

Research work on developing localised numerical models of the sanding process are very sparse. In [15], a DEM model was used to study electrical isolation, which can occur during the sanding process. In phase I of the sanding process, particles are sprayed towards the wheel–rail nip, but a large number of particles do not reach the wheel–rail contact. Therefore, the particle entrainment efficiency was studied in [16] by coupling computational fluid dynamics (CFD) and DEM. Including CFD in the analysis, clearly increases the computational time. In their analysis, the geometry was scaled down and a gap in the wheel–rail interface was introduced as it was not possible to simulate crushing of the sand particles. In [17], particle entrainment efficiency was studied in a computationally more efficient way employing DEM only. A full-scale rail-sanding set up was simulated and results were

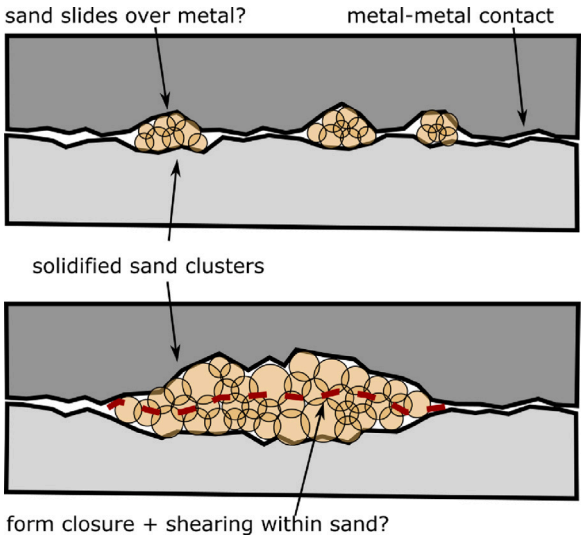

Fig. 2. Possible mechanisms for increasing adhesion via sanding.

validated using experimental data for various positions of the sander nozzle.

This study is part of a research project, where sanded contacts are experimentally investigated in detail and an advanced DEM model is to be developed to better understand the phenomena responsible for the positive effect of sand on adhesion in phase II, see Fig. 2. To separate the involved effects, the behaviour of the sand is studied first, ignoring the roughness change in the metal surfaces mentioned before. As a first step, the breakage behaviour of single sand grains was studied experimentally, [14]. For two types of rail sand, initial breakage tests and single grain crushing tests under a realistic wheel–rail contact pressure of 900 MPa were conducted.

This work presents the next steps, where a DEM model is developed to simulate the aforementioned crushing tests. In the initial breakage tests, the model needs to capture the experimentally observed differences in fragments' spread of the two types of rail sand under dry and wet contact conditions. In the high loading tests, experiments show the formation of solidified clusters of crushed material, whose size and spread differs again for the considered type of sand and contact condition. This must be reflected by the developed DEM model. Moreover, the repeated breakage under high loading conditions should not lead to an artificial loss of mass due to the chosen modelling approach.

This work is organised as follows: Section 2 gives a brief overview of particle breakage modelling in DEM. A short summary of the experimental results obtained in [14] is given in Section 3. Section 4 describes the DEM model development and contains subsections on the general material modelling and the developed breakage model. In Section 5, the calibration of the developed DEM model is presented, comparing simulations to experimental results for initial breakage tests as well as for high loading tests. Then, simulation results using the calibrated model are presented in Section 6. The last Sections contains conclusions and an outlook.

2. Literature overview on particle breakage in DEM

The DEM method has been used to model particle breakage in may applications, including confined uniaxial compression [18–20], triaxial tests [21,22], impact on particle beds [23], crushers [24] or mills [25]. There are two main modelling approaches: the agglomerate and the replacement method.

In the agglomerate method, the parent particle is modelled as agglomerate of smaller unbreakable particles, usually spheres, connected

by breakable parallel bonds, [18,19,26–31]. When the shear or tensile force at a bond exceeds its strength, the bond breaks. The agglomerate breaks into fragments of different size and shape. A drawback of this method is its high computational effort, if large specimen are considered or if the unbreakable particles involve very small sizes. Moreover, the parallel bonds introduce five additional parameters to the model, whose calibration to the breakage behaviour of a given material is a challenge frequently omitted in the literature. The big advantage of this approach is its capability to take into account both the initial shape of the parent particle, [32], as well as shape evolution during breakage, i.e. non-spherical fragments of different sizes.

The replacement method is mostly applied for granular materials represented by spheres. At first, a failure criterion must be defined to check for breakage of a sphere. This failure criterion uses the given contact forces of the particle for a simple approximation of the unknown inner stress field of the sphere. Several different failure criteria can be found in the literature, [33,34], and a comparison between frequently used criteria can be found in [35]. When the failure criterion is reached for a certain particle, this particle is replaced by an arrangement of smaller particles, called the fragment replacement modes. Different approaches have been suggested in the literature for these fragment replacement modes, [36]. To preserve the mass of the replaced particle, the daughter particles can be placed overlapping, [21], which leads to large repulsive forces due to the overlapping. If the daughter particles are placed non-overlapping, then the mass of the initial particle cannot be preserved, [22]. To compensate for mass loss, a time dependent volume increase of the daughter particles was applied in [18,33]. This approach can generate artificial contact forces with neighbouring particles. Alternatively, nearby voids can be filled with daughter particles to compensate a mass loss, [37]. To locate such voids needs a local search at every particle breakage, which increases the computational effort. In general, the replacement method is the fastest and quickest method to model particle breakage in DEM. However, when the fragmentation is not limited, the increase in the number of particles is unlimited and the decrease in their size is unlimited, which decreases the time-step size. Moreover, the replacement method cannot capture the evolution of particle shape during breakage, because the broken particle is always replaced by an arrangement of spheres.

3. Experimental sand crushing behaviour

This section summarises experimental findings published in [14], which will be used for the parametrisation of the developed DEM model.

3.1. First breakage: single grain crushing tests

Two types of rail sand were investigated, from Great Britain (GB) and Austria (AT). Single sand grains were crushed between two hardened steel plates under both dry and wet contact conditions. For GB sand, 21 tests were conducted under dry and 23 under wet conditions. For AT sand, it were 23 tests for dry and wet conditions each. In each test, photos were taken before and after crushing. Using the photos after crushing, in a post-processing step the area of fragments was determined as well as the distance from the initial position of the sand grain. A visualisation of the fragments travelled distance, d, and its area, A, can be seen in Fig. 3.

In the sanding process, the first fracture will take place several centimetres in front of the contact patch due to the narrowing gap between wheel and rail. Some of the resulting fragments are expelled from the running band (and are thus not active any more), while others stay inside and get crushed again. Therefore, it is of interest to ask how much of the mass of the initial grain would stay within a radius of 5 mm after first breakage. This radius corresponds to a typical running band half-width when the tread of a wheel is in contact with the rail head.

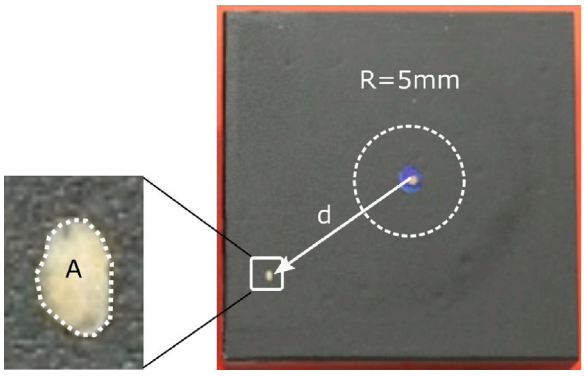

Fig. 3. Photograph taken after crushing tests including a visualisation of calculation of the distance d travelled by a fragment and its area A.

Table 1
Parameters of the fitted Weibull statistics for both GB and AT sand.

sand type	d_0 [mm]	σ_0 [MPa]	m [–]
GB	1.54	22.74	2.85
AT	1.25	22.49	2.72

This question is answered in Fig. 4. It shows cumulative histograms of the fragment distance applying a weighting by the fragment area divided by the sum of all fragments. The area of the conceptual wheel–rail contact is shown as grey box. For GB sand, the contact condition makes a big difference: under dry conditions 68% of the fragments' area stay within the conceptual wheel–rail contact, while it is 98% under wet conditions. This influence of the contact condition is less pronounced for AT sand: Even under dry conditions 93% of the fragments' area stays within the conceptual wheel rail contact and under wet conditions it is 100%.

In addition to the analysis of fragments' spread, Weibull statistics were fitted to the measured breakage force/probability of survival for GB and AT sand. No distinction between dry and wet contact condition was made, as it was assumed that the contact condition does not influence the breakage force.

The survival probability of a grain of diameter d under stress σ is described using Weibull statistics [31,38–40]:

$$P_s(d) = \exp\left[-\left(\frac{d}{d_0}\right)^3\left(\frac{\sigma}{\sigma_0}\right)^m\right], \tag{1}$$

here d_0 is the reference diameter, m is the Weibull modulus and σ_0 is the characteristic stress such that a particle of size d_0 has 37% survival probability.

A comparison of measured values from the experiment and the fitted Weibull statistics is shown in Fig. 5 for both types of sand, see e.g. [40] for details of the fitting method. The parameters of the fitted Weibull statistics are given in Table 1. The results are surprisingly similar for both types of sand, considering the differences found in the analysis of the fragment spread.

3.2. High loading: single grain crushing tests

After investigating initial grain breakage, single sand grains were crushed between hardened steel plates under realistic wheel–rail contact pressures of 900 MPa. This stress is considerably higher than in e.g. geotechnics and the condition of the sand grain after crushing is of interest. For both types of sand and for both dry and wet contact conditions, 5 tests were conducted. Before and after the test, photos were taken and after the test a non-contact imaging and measuring tool named Alicona InfiniteFocus SL was used to take high resolution 3D scans of the crushed grain.

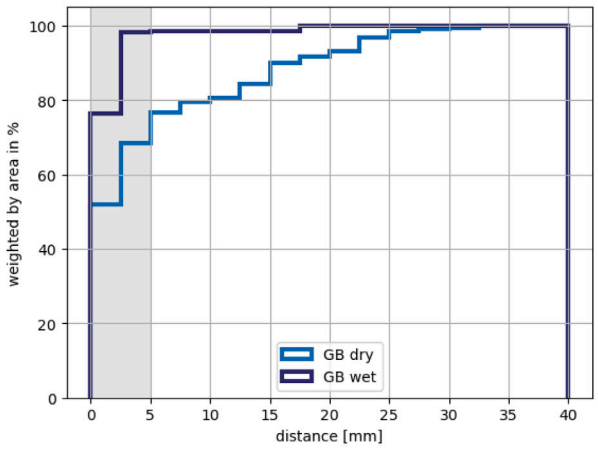

(a) GB sand

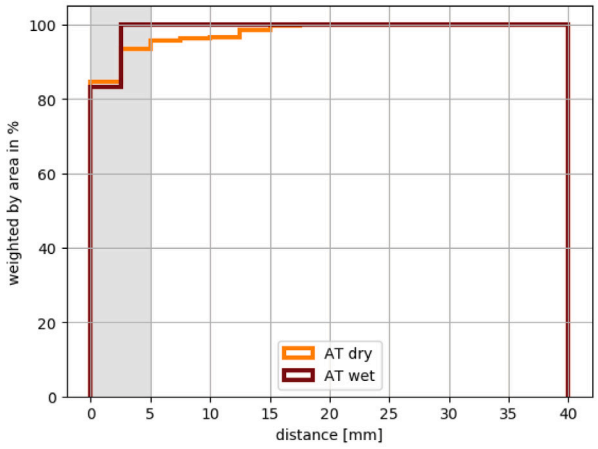

(b) AT sand

Fig. 4. Distance weighted by area for GB and AT sands. The radius of an conceptual wheel–rail contact is shaded in grey.

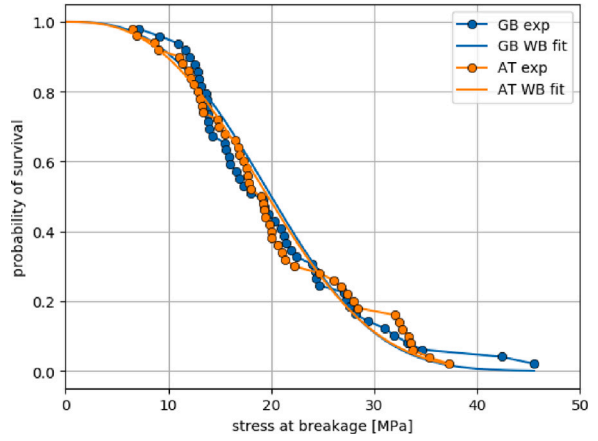

Fig. 5. Fitted Weibull statistics.

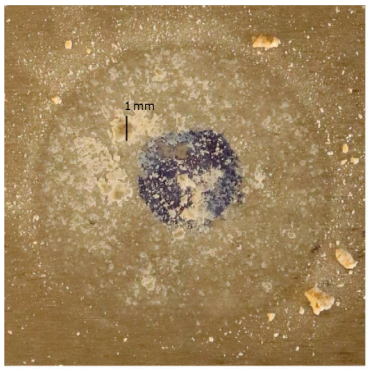

(a) photo of lower plate

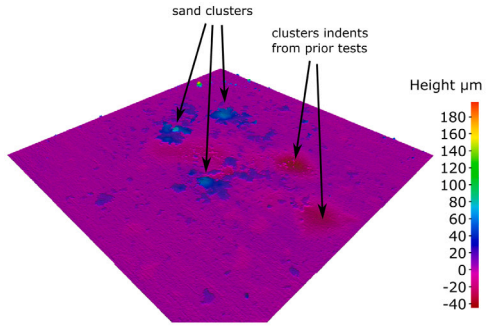

(b) Alicona scan of lower plate

(c) photo of lower plate

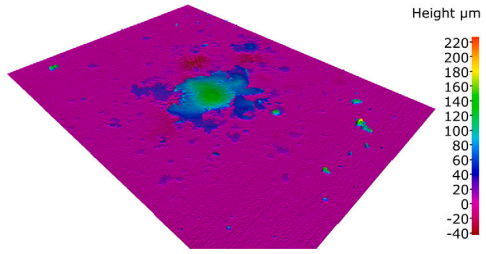

(d) Alicona scan of lower plate

Fig. 6. Example result for high load testing of GB sand under dry conditions.

In these tests, a varying amount of fragments were expelled from the contact during repeated breakage. Nevertheless, in all cases clusters of solidified sand were formed. GB sand under dry conditions showed a high variation in the amount of material, which stayed within the contact area. Examples can be seen in Fig. 6(a), Fig. 6(c) and their corresponding Alicona scans Fig. 6(b), Fig. 6(d). The smaller cluster had a length of 1 mm and a height up to 70 µm, while the larger cluster had a side length of 3.8 mm and a height up to 140 µm.

A typical result for AT sand under dry conditions can be seen in Fig. 7. This cluster has side length of about 3 mm and showed a height up to 140 µm in the Alicona scan.

Under wet conditions, both types of sand typically showed only one big cluster of solidified sand powder, see Figs. 8 and 9. The cluster of GB sand shown in Fig. 8 had a side length of 4.4 mm and a height up

(a) photo of lower plate

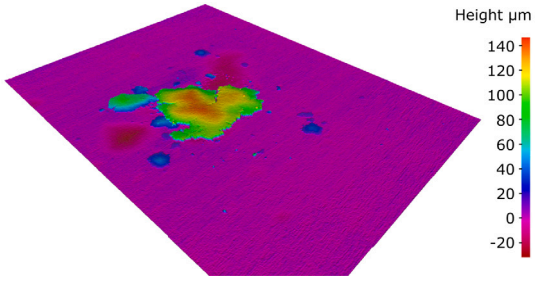

(b) Alicona scan of lower plate

Fig. 7. Example result for high load testing of AT sand under dry conditions.

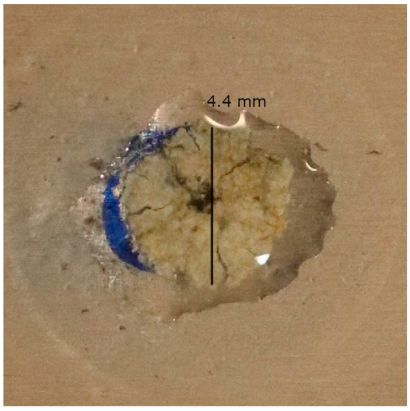

(a) photo of lower plate

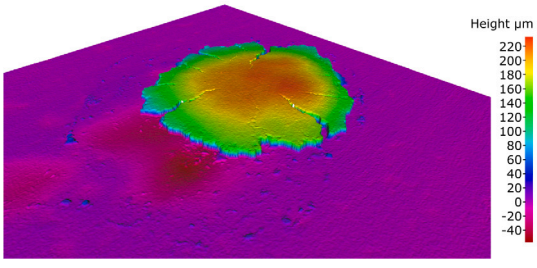

(b) Alicona scan of lower plate

Fig. 8. Example result for high load testing of GB sand under wet conditions.

to 220 µm. In contrast, the cluster of AT sand shown in Fig. 9 was much smaller with a side length of about 3 mm and heights up to 160 µm due to a smaller initial diameter of AT sand grains.

(a) photo of lower plate

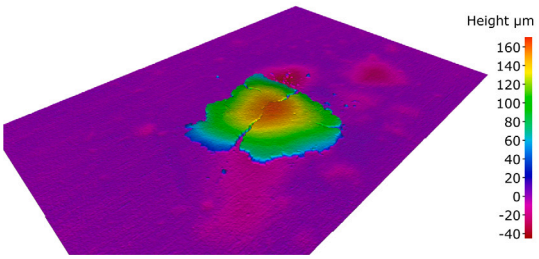

(b) Alicona scan of lower plate

Fig. 9. Example result for high load testing of AT sand under wet conditions.

4. DEM model development

For all DEM simulations in this work the software YADE [41] was used. It is Open-Source and utilises the soft contact approach together with explicit integration in time. A DEM model will be developed to simulate the described initial grain breakage tests as well as the high loading tests. In general, the aim was to find the simplest approach working, w.r.t. both computational time and number of parameters. Next, the general material modelling in DEM is described. The following subsection deals with DEM modelling of particle breakage.

4.1. DEM material modelling

The first choice to be made is about particle shape representation in the DEM model. The sand grains and their fragments are clearly non-spherical, see e.g. [19,32,42] for an accurate shape representation and related computational demands. In DEM, a computationally efficient way to mimic the behaviour of non-spherical particles is to use spheres with rolling resistance, [43–45]. The calibration of rolling resistance and inter-particle friction coefficient can lead to ambiguous parameter combinations if no proper experimental data is available, even for cohesionless material without external load, see [46]. For this work, such data on sand fragments were not available yet. Therefore, sand particles and fragments will be represented by spheres, which are not allowed to rotate. To block all rotation is computationally fast and avoids the additional rolling resistance parameter.

Next, a contact law has to be chosen for particle–particle and particle–wall contacts. In the literature, DEM simulations of sand including grain crushing frequently utilise the Hertz–Mindlin contact law, [19–22,47]. The Hertz–Mindlin contact law, including a viscous damping, [48,49], is also used in this work. The model parameters are listed in Table 2. In [50], several rail sands were characterised, including the two types considered in this work. A re-evaluation of this data provided the Young's modulus, E, of both sand types as well

Table 2
Parameters of Hertz–Mindlin contact law for considered materials.

Material	E [GPa]	ν [–]	μ [–]	$\rho \left[\frac{\text{kg}}{\text{m}^3}\right]$	e_n [–]
GB sand	86.5	0.3	0.5	2650	0.5
AT sand	79.1	0.3	0.7	2650	0.3
steel	200.0	0.28	0.4; 0.2	7833	

as the coefficient of restitution, e_n. The sands' density, ρ, was taken from the literature, see [21]. The Poisson's ratio, ν, was assumed to be 0.3. The coefficient of friction, μ, was unknown for both types of sand. In [50], the angle of repose was measured for three different types of sand, one of which was the same GB sand considered in this work. GB sand showed the lowest angle of repose of the measured sands, which can be hint of a low friction coefficient, while the angle of repose is clearly also influenced by particle shape and size. In this work, the friction coefficient is assumed to be 0.5 for GB sand, in accordance with [21], and 0.7 for AT sand. The material parameters for the steel plates were taken from literature. The coefficient of friction of the steel plates is assumed as 0.4 and 0.2 under dry and wet contact conditions, respectively.

As already mentioned in the introduction, the external loading applied during the wheel–rail sanding process is much higher than in other applications, where the crushing of sand grains occur. From the conducted tests on the initial breakage behaviour, the sand fragments' behaviour was clearly cohesionless under dry contact conditions. Under the applied high loads, the observed material behaviour changed: fragments stuck together and formed clusters of material, which deformed like one would expect from an elasto-plastic solid. Further experimental investigations are needed to improve understanding. The process is likely to be comparable to powder caking, which is complex physical process and can involve both intrinsic and extrinsic factors, [51]. The process of powder caking can be modelled in DEM by using piece-wise linear/non-linear elasto-plastic contact laws, [52–55]. These models have a higher computational effort, need to store internal states for every contact and involve at least four parameters, which makes calibration challenging. Another possibility to introduce the experimentally observed behaviour to the DEM model is to add cohesion to the Hertz–Mindlin contact law. Frequently used cohesion models are the Derjaguin–Muller–Toporov (DMT) model, [56], and the Johnson–Kendall–Roberts (JKR) model, [57,58]. Both of them involve only one cohesion parameter, γ, but the DMT model is more simple in implementation and evaluation. Therefore, the DMT model will be used in this work and the cohesive force acting on the contact is given as

$$F_{adh} = -4\,\pi\,R^*\gamma\,, \tag{2}$$

where R^* is the equivalent radius of the contact partners. To model the observed change in behaviour from cohesionless to cohesive, the cohesive force is only activated if one of the contact partners has a radius below a parameter R_γ. Both parameters, γ and R_γ will be calibrated in the simulations of high loading tests.

The DEM model described so far deals only with dry contact conditions and a computationally efficient way to consider wet contact conditions is needed. In the experiments, under wet contact conditions the spread of fragments was reduced for both the initial breakage tests and the high loading tests. An efficient way to model this effect is to add a drag force, F_{drag}, following Stokes' law to each particle, given by

$$F_{drag} = 6\,\pi\,\eta\,r\,\upsilon\,, \tag{3}$$

where r is the particle's radius, υ its velocity and η the dynamic viscosity. As the assumption for deriving Stokes law are not entirely given, e.g. Stokes law considers laminar flow, the parameter η will be calibrated to experimental results.

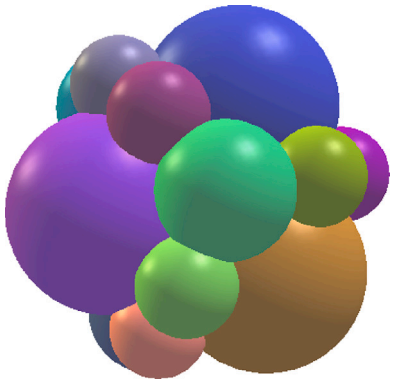

Fig. 10. Fragment replacement mode used.

4.2. DEM breakage modelling

This work uses the particle replacement method to model particle breakage. As mentioned in the introduction, it is both computationally fast and comparably easy to calibrate. At first, the particles are assigned initial strength by choosing a random probability of survival $0 < p < 1$ (using a uniform distribution). Together with the particle diameter, the Weibull statistic, (1) and Table 1, is used to calculate the strength of the initial particle. After breakage, the same probability p is used to calculate the strength of the emerging fragments. In the replacement method, a particle breakage criterion must be chosen, and in [35] four frequently used criteria are compared. The so-called F_{max} stress criterion is fast to compute and gives the correct macroscopic behaviour in [35]. Therefore, it is used in this work and it is computed as $\sigma_{Fm} = F_{max}/d^2$, where F_{max} is the largest contact normal force acting on the particle and d is the particle diameter.

If the stress on a particle exceeds its strength, then it is replaced by fragments. To avoid infinite breakage of particles, a minimal radius, R_{lim}, is introduced, below which particles are considered unbreakable. As the considered high loading tests involve a high number of repeated breakage events, it is important to avoid mass loss during replacement. To preserve the mass of the replaced particle, the fragments are placed overlapping, [21,23,24,59,60]. Fig. 10 shows the used overlapping fragment replacement mode, which consists of 20 spheres. The artificially overlapping of the fragments would lead to artificially high velocities of the fragments making the simulations unrealistic. Different numerical strategies have been proposed to prevent this problem, e.g. damping using a relaxation factor in the contact force calculation, [23,59], a global damping combined with ignoring the fragment overlap caused by fragmentation, [60], or the introduction of freezing steps to dissipate the artificial energy introduced by the fragments' initial overlap, [24]. In this work, an adaption of the freezing approach introduced by [24] will be used. Fig. 11 shows a flow chart of the chosen approach. After particle breakage, the fragment replacement mode is placed with arbitrary orientation. Fragments are assigned a coefficient of friction of 0, to allow them to move easily in both normal and tangential direction. When the system is frozen, the velocities of all particles are stored and then set to 0, the external loading is stopped and gravity is set to zero. In this phase, all particles are fixed, except those whose distance to a broken particle is less than 10 times the radius of the broken particle. In this freezing state, the free particles are allowed to move for a given time period t_0. If the maximal velocity of all particles is larger than model parameter V_b, all velocities are set to zero and the system evolves again for time period t_0. If the maximal velocity of all particles is below model parameter V_b, the system is unfrozen: all particles are free to move again, they are assigned their previous velocities, gravity and external loading is restored and the newly introduced fragments are assigned the original

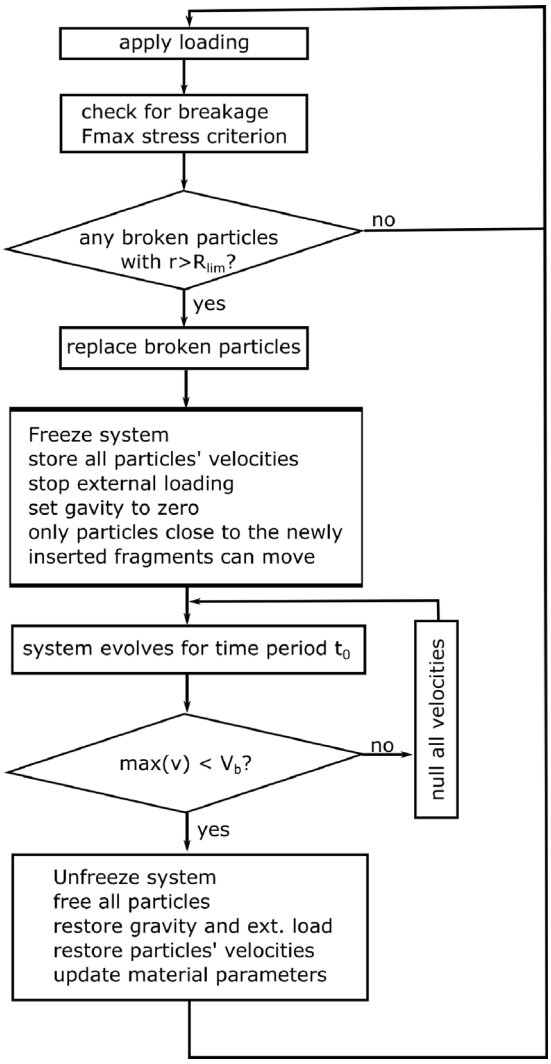

Fig. 11. Flow diagram of DEM breakage model.

value of coefficient of friction. After unfreezing the system, the loading continues. With this approach, the artificially high velocities caused by the high particle overlap, mentioned above, are controlled directly. Moreover, the spread of the fragments after breakage can be controlled via the parameter V_b. This is necessary, as the two considered types of sand show a different behaviour in their particle spread in the initial crushing experiments.

Although the presented method is not entirely physics-based it is a very efficient approach to describe the experimentally observed effects.

5. DEM model calibration

In this section, the developed DEM model will be used to simulate the initial breakage test as well as the high loading tests under dry and wet contact conditions for both types of rail sand. How the model parameters will be calibrated using these tests is outlined in the next subsection. The actual calibration and simulation results are presented subsequently.

5.1. Calibration strategy

Apart from the parameters of the contact law stated in Table 2, the developed DEM model contains the following parameters $t_0, V_b, \eta, R_{lim}, \gamma, R_\gamma$. The experiments used for their calibration are stated in Table 3.

Table 3
Parameters in the DEM model and experiments used for their calibration.

par	ini. breakage, dry	ini. breakage, wet	high load, dry and wet
t_0	x		
V_b	x		
η		x	
R_{lim}			x
γ			x
R_γ			x

In the initial breakage tests under dry conditions, the particle fractures only once and fragments are cohesionless. Therefore, under these conditions the parameters $R_{lim}, \gamma, R_\gamma, \eta$ are not active. This allows for a choice of a common value for t_0 and to calibrate V_b for each type of sand such that fragment spread in simulations and experiments are similar.

Next, the initial breakage tests under wet contact conditions can be used to find one value for η such that the experimental fragment spread is in good accordance with the simulated one for both types of sand.

The parameter R_{lim} is the radius below which spheres are not allowed to break. Measurements of particle size distributions after the high loading tests would allow for the determination of this parameter, but unfortunately such data is not available at the moment. Nevertheless, when a fragment replacement mode is given, then parameter R_{lim} can be used to calculate an upper bound for the number of fragments, assuming that all particles with a radius larger than R_{lim} would break.

The available data from the high loading tests is not sufficient for a unique calibration of parameters γ, R_γ. Additional experiments are needed to narrow down the space of possible parameter combinations or ideally to make parametrisation unique. Crushing tests at different normal loads could be helpful to see, where the formation of solidified clusters starts. From the available data, a set of parameters is searched such that simulation results and experimental results are qualitatively in good accordance.

5.2. Initial breakage tests

In the simulations of the initial breakage tests, one sand grain of the average size d_0, see Table 1, is placed between two steel plates. A probability of survival is chosen randomly between 0 and 1 (from a uniform distribution) and the corresponding strength is assigned to the particle. The loading is applied until the first breakage occurs. Then, the system goes to freeze mode. The parameter $t_0 = 10^{-7}$ s is chosen for both types of sand. When the velocity of all particles after t_0 time period is below the parameter V_b, the system is unfrozen and the particles are allowed to settle. For the initial breakage tests, 150 repetitions are simulated (using a random probability of survival) and the spread of the fragments, the travelled distance and fragment area, is evaluated in the same way as the experimental data, compare Fig. 4. In a very simple calibration, parameter V_b is varied and the corresponding simulation results for GB and AT sand are shown in Fig. 12. For the assessment of the best simulation results, the spread of the material in the conceptual area of wheel–rail contact, i.e. with a distance less than 5 mm. Thus, for GB sand $V_b = 0.12$ m/s and for AT sand $V_b = 0.08$ m/s is chosen.

The initial breakage test under wet conditions were simulated to calibrate η. Comparing GB and AT sand under dry conditions, GB sand shows higher material spread and thus, a higher value for η was needed to reach the experimentally observed small spread under wet conditions. Therefore, η was calibrated for GB sand and results for a variation of η are shown in Fig. 13(a). Simulation results for both $\eta = 0.010$ and $\eta = 0.012$ Pa s were in good agreement with the experimental results. $\eta = 0.012$ Pa s was chosen, as a higher value is beneficial in the later simulations of the high loading tests. The dynamic viscosity of water at room temperature is roughly $\eta_{water} = 0.001$ Pa s, [61]. The

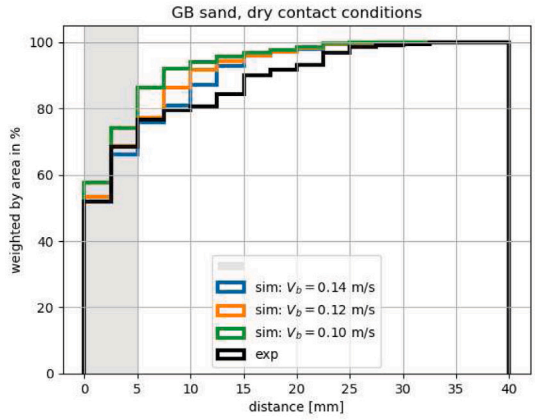

(a) GB sand

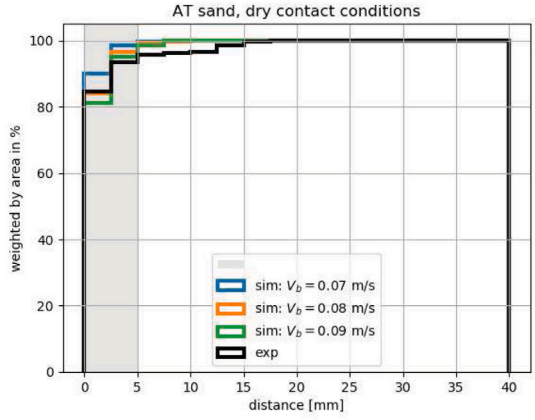

(b) AT sand

Fig. 12. Calibration of DEM model parameter V_b using initial breakage tests under dry contact conditions.

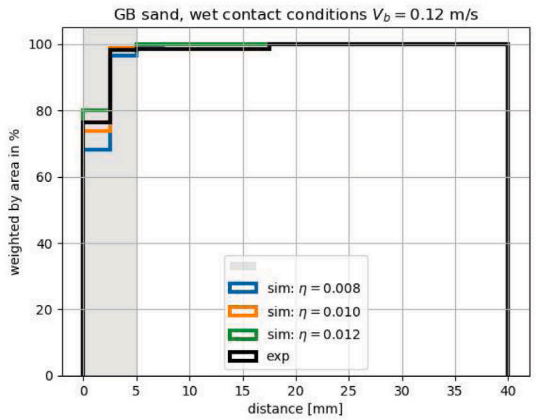

(a) GB sand

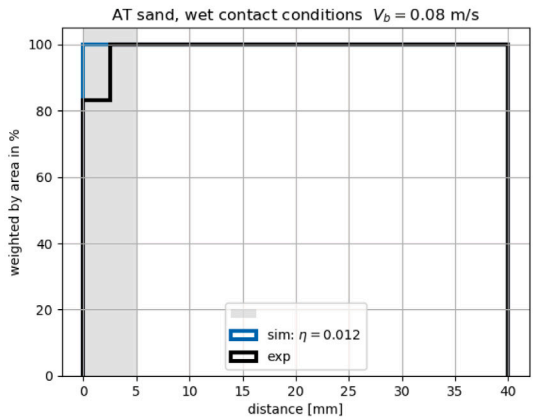

(b) AT sand

Fig. 13. Calibration of DEM model parameter η using initial breakage tests under wet contact conditions.

obtained value of η in this work was thus higher by a factor of 12. As mentioned before, not all assumptions of Stoke's law are valid and in this application the drag Force computed by Eq. (3) was seen more than a damping of the fragment's velocities. Using $\eta = 0.012$ Pa s, the initial breakage tests were also simulated for AT sand, see Fig. 13(b). The spread of sand fragments for AT sand under wet conditions was very low, already the first bin of the histogram contains 100% of all fragments. This is to be expected, as the same value of η was used in simulations of both types of sand and GB sand shows generally a higher spread of fragments than AT sand.

5.3. High loading tests

In the high loading tests, three parameters are left to calibrate: $R_{lim}, \gamma, R_\gamma$. As already mentioned, the available data is not sufficient for a unique parametrisation. The data available are the photos and height measurements from the five experiments conducted for each sand type under both dry and wet contact conditions. Additionally needed would be measurements of the fragment size distribution after the high loading test to determine R_{lim} and loading tests under varying normal load to see when the fragments' behaviour changes from non-cohesive to cohesive to determine R_γ. Some of these measurements are planned in future work.

It is an important first step to understand the influence of the different parameters on the simulation results. Therefore, a one-at-a-time variation was conducted for AT sand under dry contact conditions. In the reference run, the parameters had the following values: γ = 800 J/m^2, R_γ = 160 µm, R_{lim} = 53 µm. For the cohesion parameter, a lower value, γ = 400 J/m^2, and a higher value γ = 1600 J/m^2, were considered. In this model, cohesion was a substitute to represent the observed behaviour of cluster formation. Therefore, the values for γ were not of the same order of magnitude as for natural cohesive granular materials. R_γ is the radius, below which particles are cohesive. In the reference run, R_γ was chosen such that in the first breakage event all fragments were non-cohesive, but became cohesive from the

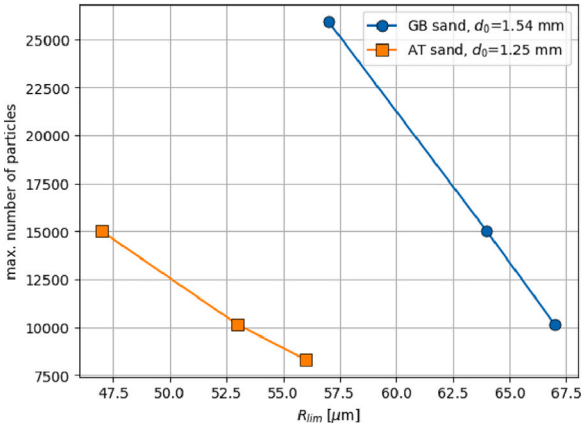

Fig. 14. Upper bound for number of particles changing with R_{lim} for both GB and AT sand.

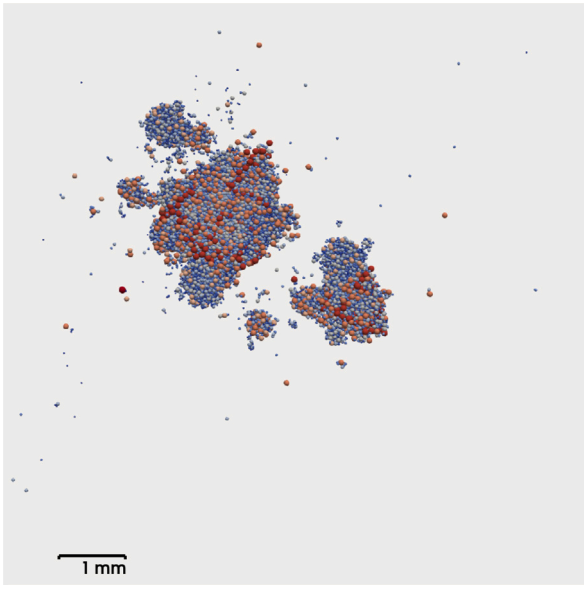

(a) reference run

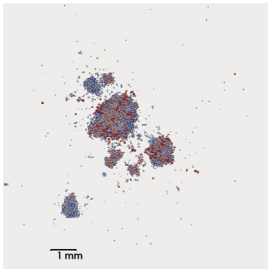

(b) $\gamma = 400$ J/m^2

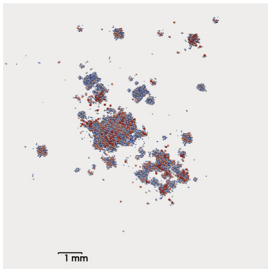

(c) R_γ=50 μm

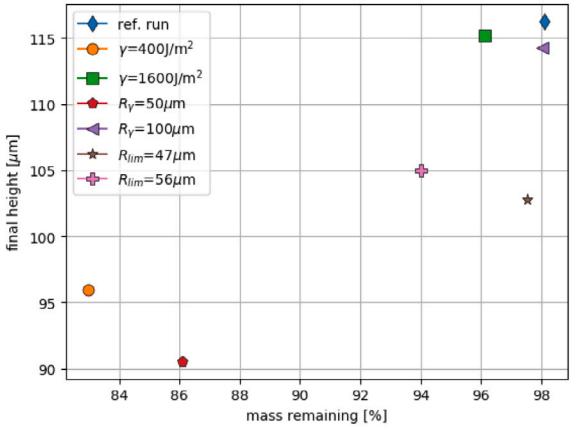

(d) specimen height and remaining mass

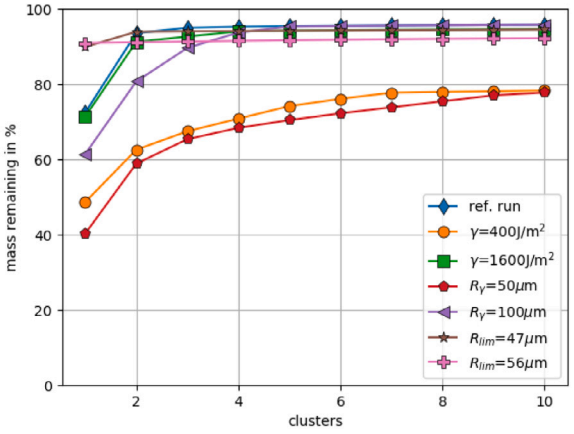

(e) cumulative mass per cluster (from largest to 10th largest)

Fig. 15. Calibration of DEM model AT sand under dry contact conditions. Parameters of reference run: $\gamma = 800$ J/m^2, $R_\gamma = 160$ µm, $R_{lim} = 53$ µm.

second breakage on. Therefore, two lower values were considered in the parameter variation, $R_\gamma = 100, 50$ µm. The parameter R_{lim} is the radius below which particles are considered unbreakable. For given R_{lim} and fragment replacement mode the maximum number of particles in the simulation could be calculated by assuming that under the applied high load all particles would fracture until they are unbreakable. This is shown in Fig. 14 for both types of sand, remember that the initial grain size was higher for GB sand than for AT sand. For R_{lim}, a lower and a higher value was considered in the one-at-a-time variation: $R_{lim} = 47, 56$ µm.

For better comparability of the results, all simulations are conducted with an initial probability of survival $p = 0.5$ and instead of inserting the fragment replacement mode at a random orientation, always the same orientation is used.

The evaluation of the obtained results is shown in Fig. 15. A top view of the reference run's result under full load can be seen in Fig. 15(a). For size comparison with other results, a 1 mm scale bar is included. The majority of fragments formed one large and three smaller clusters, while only a few fragments spread out. In these tests, the load was applied via a square plate of 10 mm side length, which corresponds to the area of wheel–rail contact. All fragments, which were expelled from this area were deleted from the simulation. Fig. 15(d) shows the relation between the total mass remaining, in percentage of the initial mass, and the final height of the specimen under full load. To get a better overview of the spreading behaviour in the samples, the forming clusters were analysed. Here, clusters were defined via the contacts in the simulations and their mass was calculated. Fig. 15(e) shows the cumulative mass (as percentage of the initial mass) of the ten largest clusters. Combining the specimen height, total mass remaining and largest cluster mass helped to understand the influence of the three parameters on the simulation results.

For parameter γ, decreasing its value to $\gamma = 400$ J/m^2, decreased the specimen height by 20 µm, the total remaining mass by 15% and the mass of the largest cluster forming by 24%. The top view of the simulation result, shown in Fig. 15(b), shows a larger spread of fragments, which can be directly related to the reduced cohesion. On the contrary, increasing cohesion to $\gamma = 1600$ J/m^2 had little effect on specimen height, reduced the mass remaining by 2% and gave nearly identical masses for the forming clusters.

Decreasing parameters R_γ to 50 µm, also strongly influenced simulation results: the specimen height was reduced by 26 µm, the total mass remaining by 12% and the mass of the largest cluster by 32%. This parameter combination gave the largest spread of fragments, which can be seen in the top view in Fig. 15(c). With a lower value of R_γ more breakage events took place before particles were considered cohesive and thus more spread was observed. When R_γ was reduced from 160 µm in the reference run to 100 µm, this increase in spread was seen only to a small extent. The specimen height and total mass were almost not affected, only the mass of the largest cluster was reduced by 11%. Both parameters γ and R_γ showed a strong influence on fragment spread and thus on the obtained size and height of forming clusters.

As mentioned before, the parameter R_{lim} directly influences the number of spheres in the simulation. From the conducted simulations, this parameter had surprisingly little influence on the obtained results: Specimen height reduced by about 12 µm for both variants and the total mass was nearly same or reduced by 4%. Only the masses of the

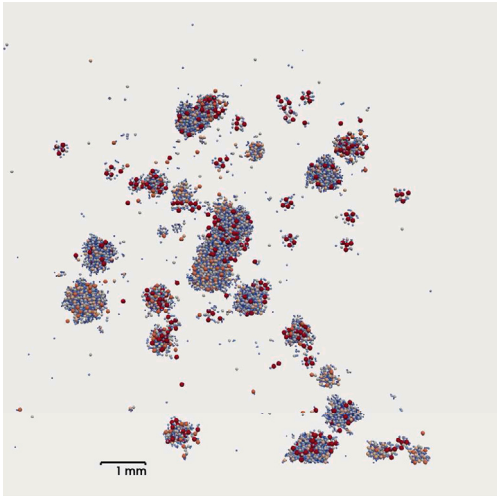

(a) example GB dry conditions

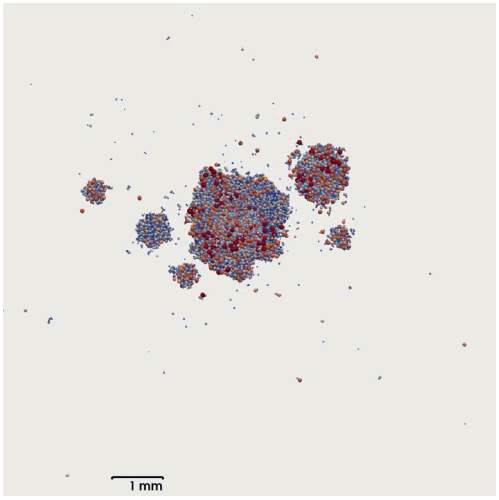

(d) example AT dry conditions

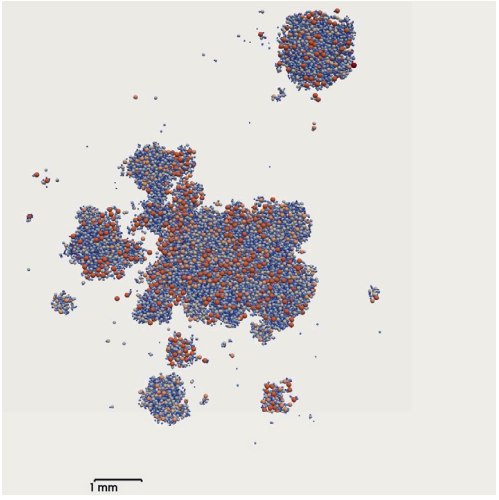

(b) example GB wet conditions

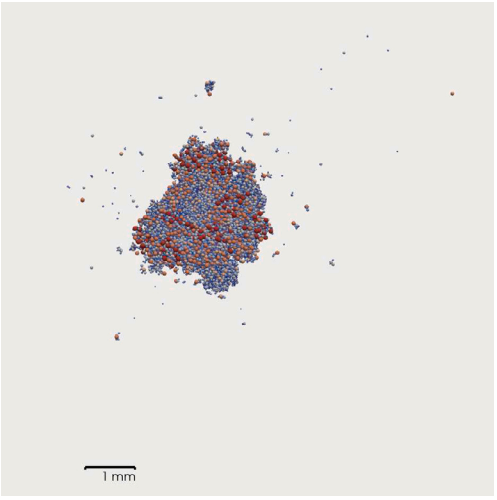

(e) example AT wet conditions

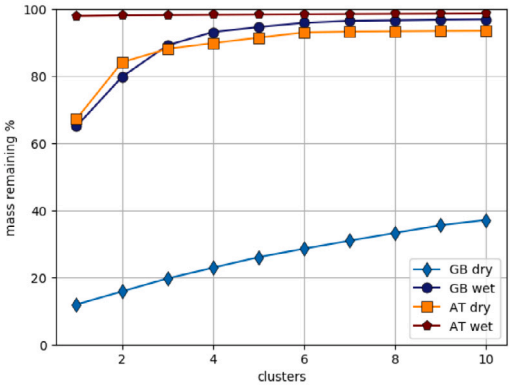

(c) cumulative mass per cluster(from largest to 10th largest)

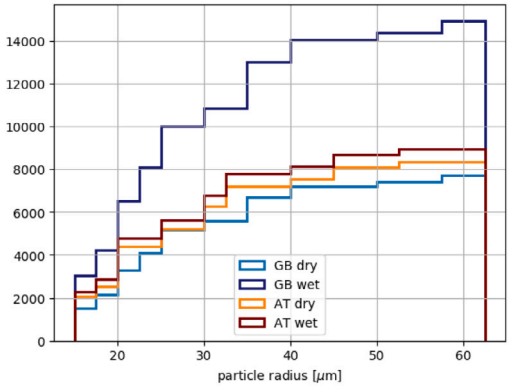

(f) cumulative histogram of particle radii

Fig. 16. Typical examples of DEM simulations of GB and AT sand under dry and wet contact conditions.

largest clusters increased by about 18% for both simulations containing more and less spheres. Thus, the influence of this parameter was not as clearly seen as in the two previous cases.

For the calibration for AT sand, the parameters must be chosen in a way to obtain little spread of fragments under dry conditions. If this is achieved, the spread will be automatically reduced under wet conditions. The parameter set of the reference run already fulfils this aim for AT sand. The value of $\gamma = 800$ J/m^2 was the lowest value

Table 4
Parameters of developed DEM model.

sand	$V_b \left[\frac{\text{m}}{\text{s}}\right]$	η [Pa s]	R_{lim} [μm]	$\gamma \left[\frac{\text{J}}{\text{m}^2}\right]$	R_γ [μm]
GB	0.12	0.012	64	800	100
AT	0.08	0.012	53	800	160

seen to avoid a strong spread of fragments. Similarly, $R_\gamma = 160$ µm is the option, which resulted in the least spread of fragments: after the initial breakage, fragments were non-cohesive, but became cohesive after following breakage events. The parameter $R_{lim} = 53$ µm limited the number of spheres in the simulation to roughly 11000. For GB sand, the aim was to obtain high spread of fragments under dry conditions and low spread of fragments under wet conditions. First, the parameter γ was chosen to be the same as for AT sand. Then, the parameter R_γ, was reduced stepwise, such that a strong spread of fragments under dry conditions was obtained, while under wet conditions the spread was low. Choosing the parameter $R_{lim} = 64$ µm resulted in a similar minimal particle size for GB and AT sand, which came at the price of nearly 15000 spheres in the simulation. The set of parameters used for both types of sand is summarised in Table 4.

6. DEM simulation results

With the chosen set of parameters, high loading tests are simulated. Due to higher computational time, the number of conducted simulations is limited. Therefore, the probability of survival of the initial grain is chosen manually to obtain better comparability between the sand types and the contact conditions. For both types of rail sand and both types of contact conditions ten simulations are conducted, with $p = 0.1, 0.5, 0.9$. Fig. 16 shows typical results obtained in the four different cases with $p = 0.5$. In addition to the obtained final configurations, Fig. 16(c) shows the corresponding analysis of the remaining mass of the ten largest clusters and Fig. 16(f) shows a cumulative histogram of the particle radii in the final configuration. GB sand under dry contact conditions, Fig. 16(a), shows a strong scatter of particles. There is a formation of clusters seen, but they remain small and are scattered over the loading area, which is also quantified in Fig. 16(c). The amount of spheres expelled can be seen in Fig. 16(f), by comparing results for wet and dry conditions. Under wet conditions, GB sand shows little particle spread, Fig. 16(b). The formation of one large cluster and five smaller clusters can be observed, compare Fig. 16(c). More than 99% of the initial mass remains in the contact area, which corresponds to the high number of spheres in Fig. 16(f). AT sand under dry conditions, Fig. 16(d), also shows little spread of fragments. The formation of one large cluster and five smaller clusters can be observed. In Fig. 16(c), the obtained results are by coincidence very similar to the case of GB sand under wet conditions. The raining mass is about 95% and the particle size distribution is given in Fig. 16(f). Under wet conditions, AT sand shows the least spread of fragments, Fig. 16(e). Only one large cluster forms, which contains more than 99% of the remaining mass, Fig. 16(c), Fig. 16(f).

For both types of sand and for dry as well as for wet contact conditions, the final configurations were in good qualitative agreement with the experimental results shown in Figs. 6 till 9. This shows the successful calibration of the developed DEM model.

The experimental results obtained show a certain scattering and in the DEM model also non-deterministic components cause a scattering, i.e. the probability of survival of the particle and the random orientation at which the fragments are inserted after breakage. This can be seen in Fig. 17, where the results of all conducted simulations are summarised, using $p = 0.1, 0.5, 0.9$. The specimen's final height over the remaining mass is shown in Fig. 17(a). The cumulative mass per cluster is shown in Figs. 17(b) and 17(c) for GB and AT sand respectively. For GB sand, the difference in both mass remaining and specimen height is quite large for most of the conducted simulations. However, two cases with similar results exist, where an unusual spread occurred under wet conditions and an unusually large cluster formed under dry conditions. Such cases with unusual results were also observed in the experimental results, [14]. For AT sand, the results obtained under dry and wet conditions are relatively similar. In general, fragments spread is lower and specimen height is larger under wet conditions. Also, for this sand type, some of the simulation results showed a stronger spread

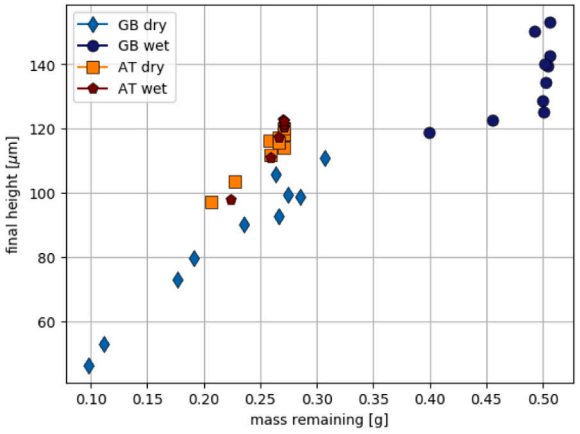

(a) final height over mass remaining

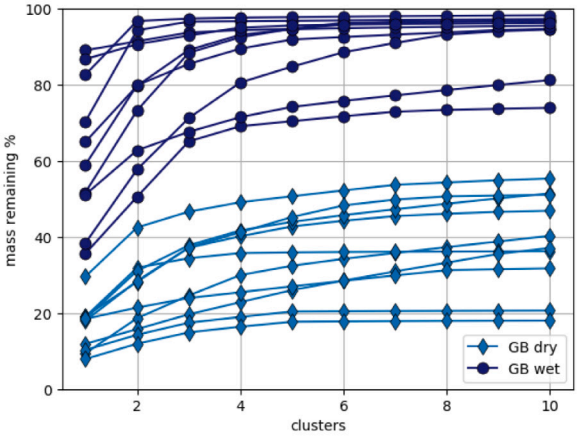

(b) GB sand: cumulative mass per cluster (from largest to 10th largest)

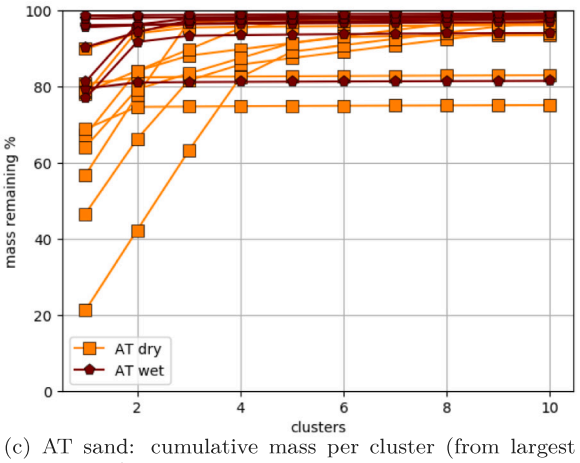

(c) AT sand: cumulative mass per cluster (from largest to 10th largest)

Fig. 17. DEM simulations of GB and AT sand under dry and wet contact conditions.

than usual, which could also be observed in the experiments. From the analysis of the results, no clear influence of the probability of survival on the final specimen height or the cumulative mass per cluster could be seen. This is most likely caused by the interaction of the DEM models other non-deterministic component, the random orientation of inserting fragments.

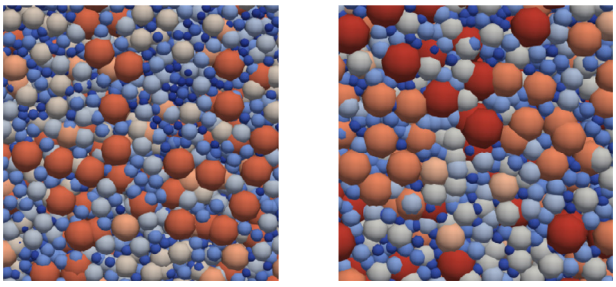

(a) GB sand: highly overlapping particles

(b) AT sand: highly overlapping particles

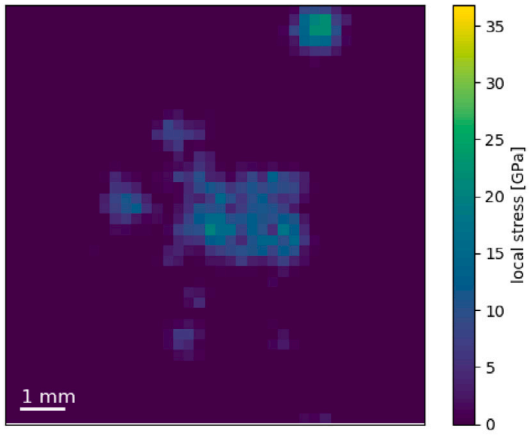

(c) GB sand: local stresses

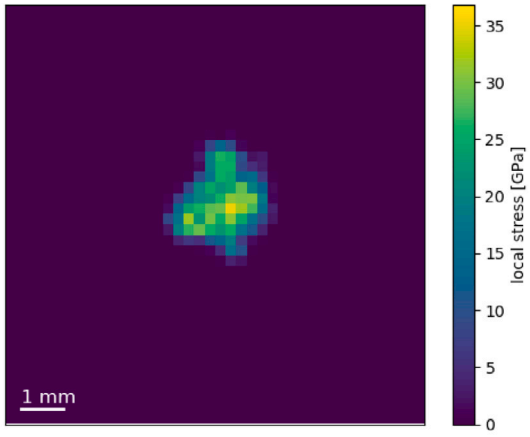

(d) AT sand: local stresses

Fig. 18. Analysis of contacts and local stresses with loading plate.

When the obtained simulation results were viewed under zoom, a problem with very high overlapping of particles became apparent. Examples are shown in Fig. 18(a) for GB sand under wet conditions and in Fig. 18(b) for AT sand under wet conditions. The observed high overlaps are clearly larger for AT sand. The reason for this behaviour is most likely related to the extremely high stresses in the wheel–rail contact. A map of local stresses is shown in Figs. 18(c), 18(d) for the final configurations shown in Figs. 16(b) and 16(e). As the sand grains of AT sand are smaller, the resulting local stresses are much higher, which shows in the observed high overlaps. To some extent, these high overlaps, will also disturb the correct calculation of obtained masses. An adaption of the developed model is ongoing work. Currently, the steel plates are simulated as non-deformable, while in experiments indentations in these plates were observed (which is also expected under realistic wheel–rail contact conditions). To simulate the steel plates as deformable objects which can form indentations and allow for force transfer between the two metal plates will reduce local stresses, which is expected to reduce the observed overlaps.

7. Conclusions and outlook

The sanding of wheel–rail contacts is a complex process, whose adhesion increasing effect is not yet understood on the level of physical mechanisms. This study is part of a research project, which tries to improve this understanding: sanded contacts are experimentally investigated in detail and an advanced DEM model is to be developed. As a first step, experiments on single sand grain crushing were conducted for two types of rail sand under dry and wet contact conditions, [14]. These experiments consisted of initial breakage tests and tests under realistic wheel–rail contact pressure of 900 MPa. In this work, a DEM model was developed, which can simulate the aforementioned experiments. After parametrisation, this model can capture the fragments' spread in the initial breakage tests for both types of sand and both dry and wet contact conditions in a quantitative comparison with the experimental results. For the high loading tests only a qualitative comparison with experiments is possible. Still, the spread of fragments and the formation of solidified clusters is similar in DEM simulation and experiments for both types of sand and both contact conditions.

The developed DEM model is not limited to study single grain crushing, but can also be used to study multiple grain interactions during crushing. This will be a mandatory step from the lab experiment towards real world application.

Future work will aim to obtain more experimental data to improve model parametrisation in the high loading tests, e.g. the application of several lower normal loads to see where the formation of solidified clusters starts. Also, for the sanding application the shearing behaviour of the two sand types is very important and small scale shear box tests are planned to be conducted. Moreover, modelling and experimental work is planned to include the observed indentations in the steel plates in the model.

CRediT authorship contribution statement

Bettina Suhr: Conceptualization, Methodology, Software, Visualization, Writing – original draft, Writing – review & editing. **William A. Skipper:** Conceptualization, Methodology, Investigations, Supervision, Writing – review & editing. **Roger Lewis:** Conceptualization, Supervision, Writing – review & editing. **Klaus Six:** Conceptualization, Methodology, Supervision, Writing – review & editing.

Declaration of competing interest

The authors declare that they have no known competing financial interests or personal relationships that could have appeared to influence the work reported in this paper.

Data availability

The dataset analysed during the current study is openly available in the zenodo.org see [62].

Acknowledgements

This research was funded in whole, or in part, by the Austrian Science Fund (FWF) project P 34273: DEM modelling of adhesion in sanded wheel–rail contacts. For the purpose of open access, the author

has applied a CC BY public copyright licence to any Author Accepted Manuscript version arising from this submission. The publication was written at Virtual Vehicle Research GmbH in Graz and partially funded within the COMET K2 Competence Centers for Excellent Technologies from the Austrian Federal Ministry for Climate Action (BMK), the Austrian Federal Ministry for Labour and Economy (BMAW), the Province of Styria (Dept. 12) and the Styrian Business Promotion Agency (SFG).

References

[1] K. Six, A. Meierhofer, G. Trummer, C. Bernsteiner, C. Marte, G. Müller, B. Luber, P. Dietmaier, M. Rosenberger, Plasticity in wheel-rail contact and its implications on vehicle-track interaction, Proc. Inst. Mech. Eng. F 231 (5) (2017) 558–569, http://dx.doi.org/10.1177/0954409716673118.

[2] O. Polach, Creep forces in simulations of traction vehicles running on adhesion limit, Wear 258 (2005) 992–1000, http://dx.doi.org/10.1016/j.wear.2004.03.046.

[3] K. Six, A. Meierhofer, G. Müller, P. Dietmaier, Physical processes in wheel-rail contact and its implications on vehicle-track interaction, Veh. Syst. Dyn. Int. J. Veh. Mech. Mob. 53 (5) (2015) 635–650, http://dx.doi.org/10.1080/00423114.2014.983675.

[4] B. White, R. Lewis, Simulation and understanding the wet-rail phenomenon using twin disc testing, Tribol. Int. 136 (2019) 475–486, http://dx.doi.org/10.1016/j.triboint.2019.03.067.

[5] G. Trummer, L. Buckley-Johnstone, P. Voltr, A. Meierhofer, R. Lewis, K. Six, Wheel-rail creep force model for predicting water induced low adhesion phenomena, Tribol. Int. 109 (2017) 409–415, http://dx.doi.org/10.1016/j.triboint.2016.12.056.

[6] L. Buckley-Johnstone, G. Trummer, P. Voltr, A. Meierhofer, K. Six, D. Fletcher, R. Lewis, Assessing the impact of small amounts of water and iron oxides on adhesion in the wheel/rail interface using high pressure torsion testing, Tribol. Int. 135 (2019) 55–64, http://dx.doi.org/10.1016/j.triboint.2019.02.024.

[7] A. Meierhofer, C. Hardwick, R. Lewis, K. Six, P. Dietmaier, Third body layer – experimental results and a model describing its influence on the traction coefficient, Wear 314 (1–2) (2014) 148–154, http://dx.doi.org/10.1016/j.wear.2013.11.040.

[8] R. Lewis, R. Dwyer-Joyce, S. Lewis, C. Hardwick, E. Gallardo-Hernandez, Tribology of the wheel-rail contact: The effect of third body materials, in: J. pombo (Ed.), Int. J. Railway Technol. 1 (1) (2012) 167–194, http://dx.doi.org/10.4203/ijrt.1.1.8.

[9] B. White, R. Nilsson, U. Olofsson, A. Arnall, M. Evans, T. Armitage, J. Fisk, D. Fletcher, R. Lewis, Effect of the presence of moisture at the wheel-rail interface during dew and damp conditions, Proc. Inst. Mech. Eng. F 232 (4) (2018) 979–989, http://dx.doi.org/10.1177/0954409717706251.

[10] R. Lewis, R. Dwyer-Joyce, J. Lewis, Disc machine study of contact isolation during railway track sanding, Proc. Inst. Mech. Eng. F 217 (2003) 11–24, http://dx.doi.org/10.1243/095440903762727311.

[11] R. Lewis, R. Dwyer-Joyce, Wear at the wheel/rail interface when sanding is used to increase adhesion, Proc. Inst. Mech. Eng. F 220 (2006) 29–41, http://dx.doi.org/10.1243/095440905X33260.

[12] W.A. Skipper, A. Chalisey, R. Lewis, A review of railway sanding system research: adhesion restoration and leaf layer removal, Tribol. Mater. Surfaces Interfaces 12 (4) (2018) 237–251, http://dx.doi.org/10.1080/17515831.2018.1542791.

[13] W. Skipper, A. Chalisey, L. R., A review of railway sanding system research: Wheel/rail isolation, damage, and particle application, Proc. Inst. Mech. Eng. F (2019) http://dx.doi.org/10.1177/0954409719851634.

[14] B. Suhr, W.A. Skipper, R. Lewis, K. Six, Sanded wheel–rail contacts: Experiments on sand crushing behaviour, Lubricants 11 (2) (2023) http://dx.doi.org/10.3390/lubricants11020038, URL https://www.mdpi.com/2075-4442/11/2/38.

[15] S. Descartes, M. Renouf, N. Fillot, B. Gautier, A. Descamps, Y. Berthier, P. Demanche, A new mechanical-electrical approach to the wheel-rail contact, Wear 265 (9) (2008) 1408–1416, http://dx.doi.org/10.1016/j.wear.2008.02.040.

[16] A. Gautam, S.I. Green, Computational fluid dynamics–discrete element method simulation of locomotive sanders, J. Rail Rapid Transit 235 (1) (2021) 12–21, http://dx.doi.org/10.1177/0954409720902897.

[17] S. Maramizonouz, S. Nadimi, W. Skipper, S. Lewis, R. Lewis, Numerical modelling of particle entrainment in the wheel–rail interface, Comput. Part. Mech. (2023) http://dx.doi.org/10.1007/s40571-023-00603-z.

[18] M.S. Bisht, A. Das, DEM study on particle shape evolution during crushing of granular materials, Int. J. Geomech. 21 (7) (2021) 04021101, http://dx.doi.org/10.1061/(ASCE)GM.1943-5622.0002067.

[19] M. Wu, J. Wang, F. Wu, DEM investigations of failure mode of sands under oedometric loading, Adv. Powder Technol. 33 (6) (2022) 103599, http://dx.doi.org/10.1016/j.apt.2022.103599, URL https://www.sciencedirect.com/science/article/pii/S0921883122001777.

[20] M. Wu, J. Wang, B. Zhao, DEM modeling of one-dimensional compression of sands incorporating statistical particle fragmentation scheme, Can. Geotech. J. 59 (1) (2022) 144–157, http://dx.doi.org/10.1139/cgj-2020-0308.

[21] J.P. de Bono, G.R. McDowell, DEM of triaxial tests on crushable sand, Granul. Matter 16 (4) (2014) 551–562, http://dx.doi.org/10.1007/s10035-014-0500-x.

[22] M.O. Ciantia, M. Arroyo, C. O'Sullivan, A. Gens, T. Liu, Grading evolution and critical state in a discrete numerical model of fontainebleau sand, Géotechnique 69 (1) (2019) 1–15, http://dx.doi.org/10.1680/jgeot.17.P.023.

[23] N. Jiménez-Herrera, G.K. Barrios, L.M. Tavares, Comparison of breakage models in DEM in simulating impact on particle beds, Adv. Powder Technol. 29 (3) (2018) 692–706, http://dx.doi.org/10.1016/j.apt.2017.12.006, URL https://www.sciencedirect.com/science/article/pii/S0921883117305009.

[24] H. Li, G. McDowell, I. Lowndes, Discrete element modelling of a rock cone crusher, Powder Technol. 263 (2014) 151–158, http://dx.doi.org/10.1016/j.powtec.2014.05.004, URL https://www.sciencedirect.com/science/article/pii/S0032591014004379.

[25] S. Bußmann, H. Kruggel-Emden, M. Reichert, Realizing fragment spawning and fragment growth in the parallelized discrete element method (DEM) during modelling of comminution, Adv. Powder Technol. 32 (7) (2021) 2171–2191, http://dx.doi.org/10.1016/j.apt.2021.04.033, URL https://www.sciencedirect.com/science/article/pii/S092188312100220X.

[26] D. Potyondy, P. Cundall, A bonded-particle model for rock, Int. J. Rock Mech. Min. Sci. 41 (8) (2004) 1329–1364, http://dx.doi.org/10.1016/j.ijrmms.2004.09.011.

[27] G.R. McDowell, O. Harireche, Discrete element modelling of soil particle fracture, Géotechnique 52 (2) (2002) 131–135, http://dx.doi.org/10.1680/geot.2002.52.2.131.

[28] Y.P. Cheng, Y. Nakata, M.D. Bolton, Discrete element simulation of crushable soil, Géotechnique 53 (7) (2003) 633–641, http://dx.doi.org/10.1680/geot.2003.53.7.633.

[29] M.D. Bolton, Y. Nakata, Y.P. Cheng, Micro- and macro-mechanical behaviour of DEM crushable materials, Géotechnique 58 (6) (2008) 471–480, http://dx.doi.org/10.1680/geot.2008.58.6.471.

[30] M.B. Cil, K.A. Alshibli, 3D assessment of fracture of sand particles using discrete element method, Geotechnique Lett. 2 (3) (2012) 161–166, http://dx.doi.org/10.1680/geolett.12.00024.

[31] I. Laufer, Grain crushing and high-pressure oedometer tests simulated with the discrete element method, Granul. Matter 17 (2015) 389–412, http://dx.doi.org/10.1007/s10035-015-0559-z.

[32] R. Fu, X. Hu, B. Zhou, Discrete element modeling of crushable sands considering realistic particle shape effect, Comput. Geotech. 91 (2017) 179–191, http://dx.doi.org/10.1016/j.compgeo.2017.07.016, URL https://www.sciencedirect.com/science/article/pii/S0266352X17301982.

[33] O. Ben-Nun, I. Einav, The role of self-organization during confined comminution of granular materials, Phil. Trans. R. Soc. A 368 (1910) (2010) 231–247, http://dx.doi.org/10.1098/rsta.2009.0205, arXiv:https://royalsocietypublishing.org/doi/pdf/10.1098/rsta.2009.0205.

[34] M. Ciantia, M. Arroyo, F. Calvetti, A. Gens, An approach to enhance efficiency of DEM modelling of soils with crushable grains, Géotechnique 65 (2) (2015) 91–110, http://dx.doi.org/10.1680/geot.13.P.218.

[35] J. de Bono, G. McDowell, Particle breakage criteria in discrete-element modelling, Géotechnique 66 (12) (2016) 1014–1027, http://dx.doi.org/10.1680/jgeot.15.P.280.

[36] W. Zhou, D. Wang, G. Ma, X. Cao, C. Hu, W. Wu, Discrete element modeling of particle breakage considering different fragment replacement modes, Powder Technol. 360 (2020) 312–323, http://dx.doi.org/10.1016/j.powtec.2019.10.002, URL https://www.sciencedirect.com/science/article/pii/S0032591019308368.

[37] O. Tsoungui, D. Vallet, J.-C. Charmet, Numerical model of crushing of grains inside two-dimensional granular materials, Powder Technol. 105 (1) (1999) 190–198, http://dx.doi.org/10.1016/S0032-5910(99)00137-0, URL https://www.sciencedirect.com/science/article/pii/S0032591099001370.

[38] W. Weibull, A statistical distribution of wide applicability, J. Appl. Mech. 18 (1951) 293–297.

[39] G.R. McDowell, M.D. Bolton, On the micromechanics of crushable aggregates, Géotechnique 48 (5) (1998) 667–679, http://dx.doi.org/10.1680/geot.1998.48.5.667.

[40] W. Lim, G. McDowell, A. Collop, The application of Weibull statistics to the strength of railway ballast, Granul. Matter 6 (2004) 229–237, http://dx.doi.org/10.1007/s10035-004-0180-z.

[41] V. Smilauer, V. Angelidakis, E. Catalano, R. Caulk, B. Chareyre, W. Chèvremont, S. Dorofeenko, J. Duriez, N. Dyck, J. Elias, B. Er, A. Eulitz, A. Gladky, N. Guo, C. Jakob, F. Kneib, J. Kozicki, D. Marzougui, R. Maurin, et al., Yade Documentation, third ed., The Yade Project, 2021, http://dx.doi.org/10.5281/zenodo.5705394, URL http://yade-dem.org/doc/.

[42] M. Wu, F. Zhou, J. Wang, DEM modeling of mini-triaxial test on soil-rock mixture considering particle shape effect, Comput. Geotech. 153 (2023) 105110, http://dx.doi.org/10.1016/j.compgeo.2022.105110, URL https://www.sciencedirect.com/science/article/pii/S0266352X22004475.

[43] K. Iwashita, M. Oda, Rolling resistance at contacts in simulation of shear band development by DEM, J. Eng. Mech. 124 (3) (1998) 285–292, http://dx.doi.org/10.1061/(ASCE)0733-9399(1998)124:3(285).

[44] C. Wensrich, A. Katterfeld, Rolling friction as a technique for modelling particle shape in DEM, Powder Technol. 217 (2012) 409–417, http://dx.doi.org/10.1016/j.powtec.2011.10.057.

[45] C. Coetzee, Calibration of the discrete element method: Strategies for spherical and non-spherical particles, Powder Technol. 364 (2020) 851–878, http://dx.doi.org/10.1016/j.powtec.2020.01.076.

[46] T. Rössler, C. Richter, A. Katterfeld, F. Will, Development of a standard calibration procedure for the DEM parameters of cohesionless bulk materials – part I: Solving the problem of ambiguous parameter combinations, Powder Technol. 343 (2019) 803–812, http://dx.doi.org/10.1016/j.powtec.2018.11.034.

[47] S. Prabhu, T. Qiu, Modeling of sand particle crushing in split hopkinson pressure bar tests using the discrete element method, Int. J. Impact Eng. 156 (2021) 103974, http://dx.doi.org/10.1016/j.ijimpeng.2021.103974, URL https://www.sciencedirect.com/science/article/pii/S0734743X21001615.

[48] Y. Tsuji, T. Tanaka, T. Ishida, Lagrangian numerical simulation of plug flow of cohesionless particles in a horizontal pipe, Powder Technol. 71 (3) (1992) 239–250, http://dx.doi.org/10.1016/0032-5910(92)88030-L, URL http://www.sciencedirect.com/science/article/pii/003259109288030L.

[49] D. Antypov, J.A. Elliott, B.C. Hancock, Effect of particle size on energy dissipation in viscoelastic granular collisions, Phys. Rev. E 84 (2011) 021303, http://dx.doi.org/10.1103/PhysRevE.84.021303, URL http://link.aps.org/doi/10.1103/PhysRevE.84.021303.

[50] W. Skipper, S. Nadimi, A. Chalisey, R. Lewis, Particle characterisation of rail sands for understanding tribological behaviour, Wear 432–433 (2019) 202960, http://dx.doi.org/10.1016/j.wear.2019.202960.

[51] U. Zafar, V. Vivacqua, G. Calvert, M. Ghadiri, J. Cleaver, A review of bulk powder caking, Powder Technol. 313 (2017) 389–401, http://dx.doi.org/10.1016/j.powtec.2017.02.024, URL https://www.sciencedirect.com/science/article/pii/S0032591017301511.

[52] S.C. Thakur, H. Ahmadian, J. Sun, J.Y. Ooi, An experimental and numerical study of packing, compression, and caking behaviour of detergent powders, Particuology 12 (2014) 2–12, http://dx.doi.org/10.1016/j.partic.2013.06.009, URL https://www.sciencedirect.com/science/article/pii/S167420011300179X, Special issue on conveying and handling of particulate solids – Challenges of discrete element simulation, application and calibration.

[53] J. Horabik, J. Wiacek, P. Parafiniuk, M. Stasiak, M. Bańda, M. Molenda, Tensile strength of pressure-agglomerated potato starch determined via diametral compression test: Discrete element method simulations and experiments, Biosyst. Eng. 183 (2019) 95–109, http://dx.doi.org/10.1016/j.biosystemseng.2019.04.019, URL https://www.sciencedirect.com/science/article/pii/S1537511018312844.

[54] Y. Gao, G. De Simone, M. Koorapaty, Calibration and verification of DEM parameters for the quantitative simulation of pharmaceutical powder compression process, Powder Technol. 378 (2021) 160–171, http://dx.doi.org/10.1016/j.powtec.2020.09.019, URL https://www.sciencedirect.com/science/article/pii/S0032591020308834.

[55] C. Eichler, S. Pietsch-Braune, M. Dosta, A. Schmidt, S. Heinrich, Micromechanical analysis of roller compaction process with DEM, Powder Technol. 398 (2022) 117146, http://dx.doi.org/10.1016/j.powtec.2022.117146, URL https://www.sciencedirect.com/science/article/pii/S0032591022000407.

[56] B. Derjaguin, V. Muller, Y. Toporov, Effect of contact deformations on the adhesion of particles, J. Colloid Interface Sci. 53 (2) (1975) 314–326, http://dx.doi.org/10.1016/0021-9797(75)90018-1, URL https://www.sciencedirect.com/science/article/pii/0021979775900181.

[57] K.L. Johnson, K. Kendall, R.A. D., Surface energy and the contact of elastic solids, Proc. R. Soc. Lond. Ser. A Math. Phys. Eng. Sci. 324 (1971) 301–313, http://dx.doi.org/10.1098/rspa.1971.0141.

[58] K. Johnson, Contact Mechanics, Cambridge University Press, 1985.

[59] G.K. Barrios, N. Jiménez-Herrera, L.M. Tavares, Simulation of particle bed breakage by slow compression and impact using a DEM particle replacement model, Adv. Powder Technol. 31 (7) (2020) 2749–2758, http://dx.doi.org/10.1016/j.apt.2020.05.011, URL https://www.sciencedirect.com/science/article/pii/S092188312030203X.

[60] L.M. Tavares, V.A. Rodriguez, M. Sousani, C.B. Padros, J.Y. Ooi, An effective sphere-based model for breakage simulation in DEM, Powder Technol. 392 (2021) 473–488, http://dx.doi.org/10.1016/j.powtec.2021.07.031, URL https://www.sciencedirect.com/science/article/pii/S003259102100615X.

[61] J.R. Rumble (Ed.), CRC Handbook of Chemistry and Physics, ninety ninth ed., CRC Press, 2018.

[62] B. Suhr, K. Six, W. Skipper, R. Lewis, Single Grain Crushing Tests on Two Sand Types Used for Wheel-Rail Sanding [Data set], Zenodo, 2023, http://dx.doi.org/10.5281/zenodo.7547518.